CrossMark

HST UV Observations of Asteroid (16) Psyche

Tracy M. Becker[1] , Nathaniel Cunningham[2] , Philippa Molyneux[1] , Lorenz Roth[3] , Lori M. Feaga[4] ,
Kurt D. Retherford[1,5] , Zoe A. Landsman[6] , Emma Peavler[1,7], Linda T. Elkins-Tanton[8] , and Jan-Erik Walhund[9]
[1] Southwest Research Institute, 6220 Culebra Road, San Antonio, TX 78238, USA; Tracy.Becker@swri.org
[2] Nebraska Wesleyan University, Lincoln, NE, USA
[3] KTH Royal Institute of Technology, Stockholm, Sweden
[4] University of Maryland, College Park, MD, USA
[5] University of Texas San Antonio, San Antonio, TX 78249, USA
[6] Florida Space Institute, University of Central Florida, Orlando, FL, USA
[7] University of California Los Angeles, Los Angeles, CA, USA
[8] Arizona State University, Tempe, AZ, USA
[9] Swedish Institute of Space Physics, Uppsala, Sweden

Abstract

The Main Belt Asteroid (16) Psyche is the target object of the NASA Discovery Mission Psyche. We observed the asteroid at ultraviolet (UV) wavelengths (170–310 nm) using the Space Telescope Imaging Spectrograph on the Hubble Space Telescope during two separate observations. We report that the spectrum is very red in the UV, with a blue upturn shortward of ∼200 nm. We find an absorption feature at 250 nm and a weaker absorption feature at 275 nm that may be attributed to a metal-oxide charge transfer band. We find that the red-sloped, relatively featureless spectrum of (16) Psyche is best matched with the reflectance spectrum of pure iron; however, our intimate mixture models show that small grains of iron may dominate the reflectance spectrum even if iron only comprises up to 10% of the material on the surface. We also stress that there is a limited database of reflectances for planetary surface analogs at UV wavelengths for comparison with the spectrum of (16) Psyche. The mid- and far-UV spectra (<240 nm) are markedly different for each of the four asteroids observed at these wavelengths so far, including ones in the same spectral class, indicating that UV observations of asteroids could be used to better understand differences in the composition and processing of the surfaces of these small bodies.

1. Introduction

The asteroid (16) Psyche (hereafter, Psyche) is the target of the NASA Discovery Mission Psyche, expected to launch in 2022 (Elkins-Tanton et al. 2017). Psyche is the largest of the asteroids designated as an M-type in the Tholen taxonomic classification (Tholen 1984), which are defined by their featureless, red-sloped spectra in the visible and near-infrared (near-IR) wavelengths. The relatively higher radar albedo measurements of many M-types suggest a composition dominated by iron–nickel (Ostro et al. 1985; Shepard et al. 2008, 2010), leading to the hypothesis that these asteroids are the remnant metallic cores of larger, differentiated protoplanets, exposed after a series of hit-and-run collisions stripped the bodies of their mantles (Chapman & Salisbury 1973; Bell et al. 1989); Asphaug et al. 2006; Asphaug 2010; Sarid et al. 2015). Psyche is the archetype of this class of asteroids.

The shape, effective diameter (226 ± 23 km), and radar albedo (0.37 ± 0.09) of Psyche were derived from observations taken by the Arecibo Observatory (Shepard et al. 2017). These measurements, combined with estimates of its mass ((2.72 ± 0.75) × 10^{19} kg) from observations of gravitational perturbations on other asteroids (Viateau 2000; Kuzmanoski & Kovačević 2002; Carry 2012), indicate that its bulk density is $\sim 3990 \pm 260\,\mathrm{kg/m^{-3}}$, consistent with an Fe–Ni composition with 40% macroporosity or

a stony iron with almost no macroporosity (Britt & Consolmagno 2003; Viikinkoski et al. 2018). However, initial estimates of an elevated thermal inertia that would be indicative of high metal content (Matter et al. 2013) may be contradicted by a more moderate thermal inertia derived using data from the Spitzer Space Telescope (Landsman et al. 2017).

In the Bus-DeMeo asteroid taxonomy (DeMeo et al. 2009), Psyche is classified as Xk due to the presence of an absorption feature at 0.95 μm (Hardersen et al. 2005) attributed to orthopyroxenes on the surface. IR studies using the NASA Infrared Telescope Facility (IRTF) measured a 3 μm absorption feature, which was attributed to water or OH (hydroxyl) on the surface (Takir et al. 2017), though measurements from the AKARI satellite did not detect this feature (Usui et al. 2019). An absorption feature has also been observed at 0.43 μm on Psyche, which may be associated with chlorites and magnesium-rich serpentines or pyroxenes (Fornasier et al. 2010). The presence of these materials suggests a possible alternate formation scenario for Psyche or has implications for exogenic material emplaced on the asteroid's surface. Despite the noted absorption features, the current best meteorite analog for Psyche based on visible and IR observations is the relatively featureless iron meteorite MET101A (Fornasier et al. 2010).

To better assess the composition of Psyche, we consider the ultraviolet (UV) spectrum of the asteroid. Laboratory studies by Cloutis et al. (2008) show that the UV spectral region can be more sensitive to some mineral properties than the longer wavelengths and can therefore be extremely useful in the compositional analysis of planetary surfaces. Although it is a
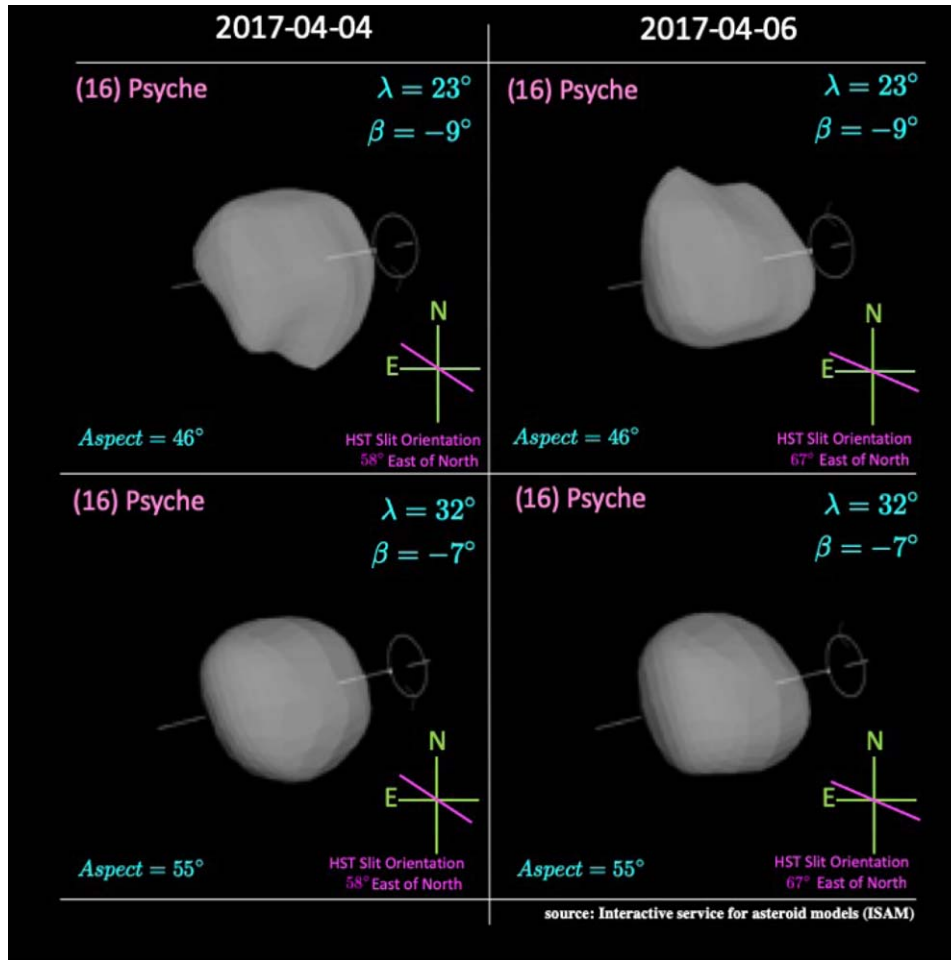
Figure 1. Orientation of Psyche at the time of the two HST observations assuming the shapes and pole orientations determined by Hanuš et al. (2017; top row) and Kaasalainen et al. (2002; bottom row). The data were taken 12.499 rotations apart and observe different longitudes on the surface, though the relative orientation of the asteroid was such that much of the northern hemisphere was observed during both data acquisitions. The angular size of Psyche was $\sim0\rlap{.}{''}13$ for both observations, well within the $0\rlap{.}{''}2$ width of the slit. Along the slit, Psyche occupies ~5 pixels, using the $0\rlap{.}{''}025$ plate scale for STIS. Figures were generated using the Interactive Service for Asteroid Models found at http://isam.astro.amu.edu.pl/ (Marciniak et al. 2012).

target of significant interest, Psyche had not been observed in the UV since the asteroid observation campaign conducted by the International Ultraviolet Explorer (IUE) in the 1980s (Butterworth & Meadows 1985).

Here we report the analysis of high-resolution UV observations of Psyche taken in 2017 April by the Space Telescope Imaging Spectrograph (STIS) on the Hubble Space Telescope (HST) that extends the spectral coverage of Psyche down to ~170 nm. In Sections 2 and 3 we discuss the observations and data reduction, with a discussion of our analysis of the data in Section 4. We present potential spectral analogs to Psyche in Section 5. In Section 6 we consider implications for the surface composition of Psyche and the need for more UV observations of asteroids. We summarize our findings in Section 7.

2. Observations

We observed Psyche on 2017 April 4 and 6 using the HST STIS first-order NUV Multi-Anode Microchannel Array (MAMA) G230L grating mode with the $52 \times 0\rlap{.}{''}2$ slit. The bandpass for this grating is 158–310 nm, though the signal-to-noise ratio (S/N) shortward of 170 nm is very low for these observations. The observations were taken such that Psyche, which has a rotation period of ~4.2 hr, had rotated 12.499 times between the HST visits. This was planned so that

comparisons could be made between hemispheres, though the orientation of the pole angle relative to the Earth meant that much of the northern hemisphere was observed in both observations, as shown in Figure 1. Each hemisphere was observed for the duration of one HST orbit after acquisition, resulting in exposure times of 2288 s or approximately $54°$ of the asteroid's rotation. The HST slit was oriented $58°$ and $67°$ east of north on the first and second observation, respectively. Details of the observations are included in Table 1.

Psyche was at a distance of 2.40 and 2.42 au from the Earth during the first and second HST visits, resulting in an angular diameter of $0\rlap{.}{''}130$ and $0\rlap{.}{''}129$, respectively. The $0\rlap{.}{''}025$ plate scale of the STIS NUV mode meant that we collected signals across the asteroid's diameter over ~5 pixels, enabling a simple analysis of potential spatial variability.

3. Data Reduction

The raw 2D spectra were reduced to calibrated, background-subtracted 1D flux spectra ("x1d" files) by the HST software pipeline, using CALSTIS software version 3.4.1. This processing is designed for sources that are pointlike at the STIS resolution. Though Psyche is not a point source, its $0\rlap{.}{''}130$ diameter, covering 5 spatial pixels on the STIS MAMA detector, is well contained within the $0\rlap{.}{''}2$ wide slit and 11 pixel

Table 1
HST Observations of Psyche

Visit	Data Set	Obs Date (YYYY-MM-DD)	Obs Time (HH:MM:SS)	Exp Time (s)	Phase Angle (deg)	Geocentric Distance (au)
1	od8 × 02010	2017-04-04	01:02:42	2288	10.75	2.400
2	od8 × 54010	2017-04-06	05:39:32	2288	11.34	2.420

high spectral extraction region. Aligning the spectral features (of solar origin) in common between the spectra from the two visits required shifting the wavelength scale of the first visit by −0.12 nm; wavelength scales of both spectra were further shifted by −0.07 nm to best match the solar spectra described below, in order to minimize artifacts when dividing. These two shifts cannot be accounted for by expected Doppler shifts, as the pipeline already corrects for Doppler shifts due to HST's orbital motion and the motion of Earth around the Sun; and the difference in radial velocity of Psyche with respect to the Sun between these two visits is too small to account for such a shift. For present purposes, with fluxes subsequently binned in 1 nm or wider bins, such shifts are negligible. We binned the 1D flux spectra to improve S/N into 1 and 3 nm bins (from the pipeline's original 0.16 nm bins for this observing mode). Flux uncertainties of 1σ including statistical and instrumental contributions were also produced by the pipeline and propagated in the binning process.

We used solar flux spectra from the Solar Radiation and Climate Experiment (SORCE)/Solar–Stellar Irradiance Comparison Experiment (SOLSTICE) instrument (McClintock et al. 2005) acquired on dates matching those of our STIS observations but was shifted by one day to correct for solar rotation. The solar spectra were binned in the same fashion as the STIS spectra and were used to calculate geometric albedo p in each wavelength bin according to Equation (1):

$$p = \left(\frac{F(\lambda)_P}{F(\lambda)_{\mathrm{Sun}}} \right) \frac{D^2 \Delta^2}{R_P^2 (1 \ \mathrm{au})^2} f \tag{1}$$

where D is the Earth–Psyche distance in astronomical units, Δ is Sun–Psyche distance in km, $R_P = 113$ km is the effective radius of Psyche, f is a unitless phase correction factor, $F(\lambda)_P$ is the flux of Psyche from STIS at each wavelength, and $F(\lambda)_{\mathrm{Sun}}$ is the SOLSTICE solar flux observed at 1 au at each wavelength, where the flux is given in erg cm^{-2} s^{-1} Å^{-1}. We assume a phase curve similar to that measured at visible wavelengths, which would indicate a phase correction factor of 1.8 for these observations (Lupishko et al. 1980). This is also consistent with the rough UV phase curve for Psyche presented by Roettger & Buratti (1994) with corrections made using IUE spectra of Psyche by Butterworth & Meadows (1985), though the wavelength-dependent phase curve could be different at shorter wavelengths. The 3% uncertainty in the SOLSTICE-measured solar flux (Sparn et al. 2005) has not been included in these albedo calculations.

We present the derived geometric UV albedo of Psyche in Figure 2, binned to spectral resolutions of 1 nm and 3 nm. Here we average the spectra from both HST STIS data sets. The error bars represent the 1σ propagated uncertainties from the averaged spectrum of Psyche. We overplot an inverted solar spectrum on the 1 nm resolution plot for reference. The apparent outlier data points near 280 and 285 may be explained by the inadequate removal of the Mg II doublet near 280 nm

and the Mg I line at 285.2 nm in the solar spectrum. The outliers at longer wavelengths may be due to the series of sharp solar features longward of 290 nm.

Psyche's UV spectrum is red overall with an albedo minimum near 200 nm and a blue slope shortward of ∼200 nm. Inspection of Figure 2(b) reveals possible absorption features in the spectrum near 250 and 275 nm. There is also a potential feature centered near 220 nm; however, its proximity to the FUV upturn at 200 nm makes it hard to distinguish from the broader spectral shape and thus we do not attempt to measure it in this work. Our spectral analysis of Psyche relies on the broader features and the slope of the spectrum, so we will use the 3 nm spectral binning for reference hereafter, unless otherwise explicitly stated. Similarly, our analysis will use the geometric albedo derived from the combination of the data, as shown in Figure 2(b), from the two HST visits, except when explicitly stated.

4. Data Analysis

For our analysis of Psyche, we assess potential spatial heterogeneity of the asteroid's surface, identify and measure spectral features, and compare the UV spectrum with spectral mixing models in order to better understand the surface composition of the asteroid. We note that observations at mid-UV wavelengths (∼200–300 nm) have a sensing depth of tens to hundreds of nanometers and so our study is of the uppermost surface layer.

4.1. Surface Variability

As discussed in Section 2, we designed the two HST observations so that we could observe nearly opposite hemispheres of Psyche in order to look for variations in brightness or spectral features. In Figure 3 we show the spectra from each visit, binned to 3 nm spectral resolution, as well as the ratio between the data sets. Longward of 200 nm, the slopes and locations of spectral features (Section 4.2) are very similar. This is consistent with the lack of statistically significant rotational variation in the metal abundance in the visible—near-IR study of Psyche completed by Sanchez et al. (2017), though that study observed the opposite hemisphere than these observations. We note, however, that Takir et al. (2017) did find rotational variability in the 3 μm feature. Both UV spectra appear to display an upturn into the FUV, where the reflectance increases with decreasing wavelengths. However, for Visit 2, the upturn occurs near 200 nm, while for Visit 1 the upturn occurs closer to 180 nm, where the data is noisier. The position of this upturn may be related to space weathering or differences in the composition or roughness of the surface (see Section 4.4).

We note that our observations do not cover the southern hemisphere of Psyche, where a mass-deficit region was detected by radar observations (Shepard et al. 2017) and where rotational variations in the pyroxene chemistry were observed by Sanchez et al. (2017). Further, these variations were detected using subtle differences in the band depth and location
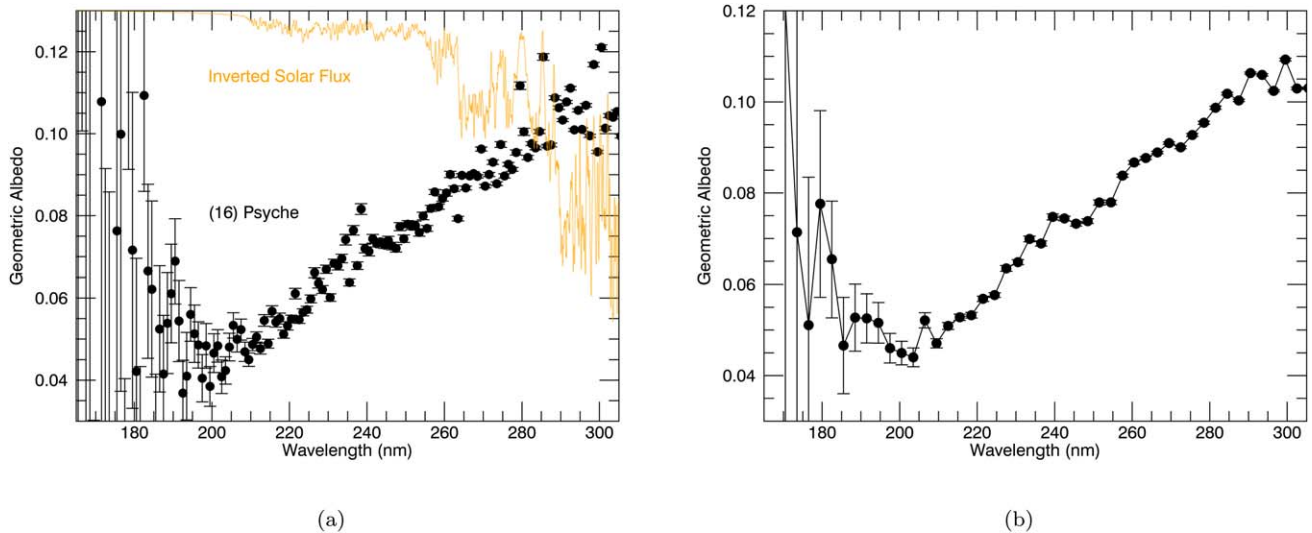
(a)

(b)

Figure 2. UV spectrum of Psyche binned to 1 nm (left) and 3 nm (right) spectral resolution, with 1σ uncertainties. We overplot the inverted solar spectrum in orange to show where solar features may not have been adequately removed during the data reduction, resulting in several outlier points at wavelengths longer than 270 nm.
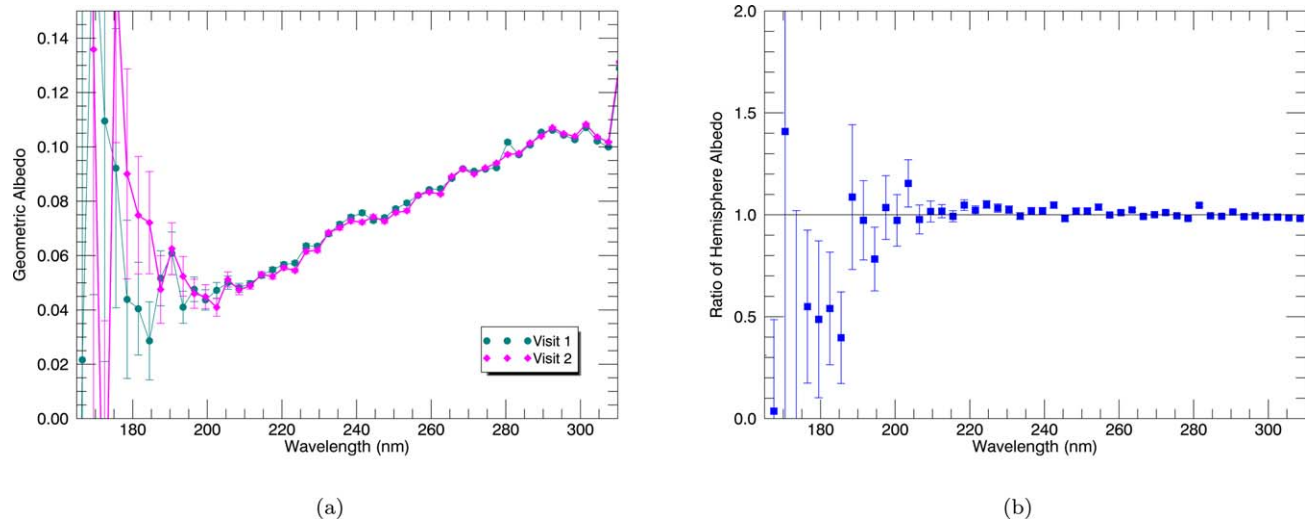

(a)

(b)

Figure 3. Comparison between observed hemispheres of Psyche. At longer wavelengths, the hemispheres appear to have very little heterogeneity. Differences are more apparent at wavelengths <200 nm, where the FUV upturn begins, which is potentially indicative of composition, space weathering, or a combination of the two; however, this region is also much noisier than in the NUV.

of the 0.9 micron feature at eight different rotation phases. With only two rotation phases, we do not detect significant changes but also do not rule out the possibility of small longitudinal variations.

We were able to spatially resolve Psyche across ∼5 spectral pixels. To further assess spatial variability of the asteroid, we use the calibrated, background-subtracted 2D spectral images produced by calstis ("x2d" files). We assume the brightest 4 pixels contain the majority of the signal from Psyche and compare the two sides of the asteroid captured within the field of view by summing the top 2 and bottom 2 pixels along the slit containing that signal. The line spread function for the STIS MAMA grating at a wavelength of 240 nm for both an extended source and a point source is ∼2 pixels; thereby we encompass the entire line spread function in the summed signal. In Figure 4, we show the ratio of the two sides during each visit. Here we focus on wavelengths longer than 200 nm because of the lower S/N in the FUV. Visit 2 may have a somewhat sharp difference in spectra near 250 nm, which may

be attributed to the strength of the Fe–O charge transfer band (see Section 4.2). Both visits show some small spectral difference between the sides near 300 nm, perhaps suggesting a feature in the northern hemisphere, since that side of the asteroid was captured during both visits due to the asteroid orientation (Figure 1). There is a difference, however, in the position of the FUV upturn along the slit during Visit 1 (see Section 4.4). These differences may suggest variability of the composition of the uppermost surface layer of Psyche.

4.2. Absorption Features

As discussed in Section 3, we identified two clear spectral features centered near 250 and 275 nm. To measure the strength of these features, we determine the background continuum slope by fitting a line to the spectrum on either side of the feature and then dividing by that baseline to remove the local continuum. For the 250 nm feature, we use the average albedo between 233.5 and 239.5 nm and between 257.5 and 263.5 nm to establish the baseline (Figure 5(a)). For
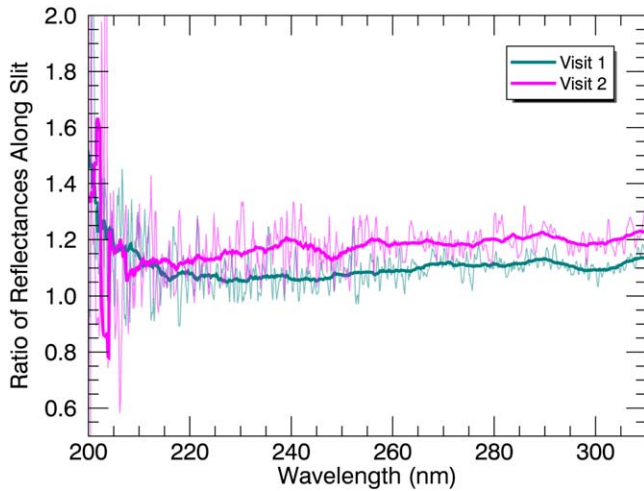
Figure 4. Ratio of the upper two and lower two STIS pixels containing data of Psyche for each visit, smoothed using a boxcar average. For Visits 1 and 2, the FUV upturn appears to differ along the slit. For Visit 2, there may also be a difference in the strength of a feature at 250 nm. Both visits show a possible weak feature near 300 nm in only one half of the slit. In both visits the bottom of the slit, which mostly captures the northern hemisphere of Psyche, has a lower reflectance than the more equatorial region that is rotating through the top of the slit by approximately 10% and 20% for Visit 1 and 2, respectively.

the 270 nm feature, we find the average albedo between 263.5 and 269.6 nm and between 284.5 and 290.5 nm to find the baseline (Figure 5(c)).

After dividing by the established baseline for the local spectral slope, we then fit a parabola to the data points that fall below the average continuum (Figures 5(b) and (d)). Using the minima of those parabolas, we determine estimates for the band depth and position of the feature.

We find that the first absorption feature is centered at 249.8 nm with a band depth of ∼5.6% and an approximate bandwidth of 18 nm. We measure a sharper, shallower second absorption feature near 275 nm. Assuming the fitted parabola minimum as the band center and depth, we find that it is centered at 275.6 nm with a band depth of 2.5%. However, a parabola does not produce a good fit to this feature, which presents itself more like the check mark-shaped absorption features sometimes detected at 3 μm on asteroids (Landsman et al. 2015). If we instead assume the lowest data point represents the band center and depth, the absorption feature is centered at 272.5 nm with a band depth of 3.3% and a bandwidth of approximately 13 nm.

Laboratory observations of a variety of minerals show a number of spectral features in the UV (e.g., Wagner et al. 1987; Cloutis et al. 2008). While many of the materials measured by Cloutis et al. (2008) displayed bands at 250 nm or 275 nm, no single material they investigated displayed bands at both of those wavelengths. An absorption feature near 250 nm is consistent with Fe^{2+}–O or Ti^{4+}–O charge transfer bands (Cloutis et al. 2008). Most of the materials (some pyroxenes, olivines, and plagioclase feldspars) with a 275 nm minimum in the Cloutis et al. (2008) study had another reflectance minima between 220 and 225 nm. It is possible that a very weak 220 nm absorption feature can be seen in the Psyche spectrum, but it is not distinguishable from the slope of the spectrum.

4.3. Previous UV Spectra of Psyche

Previous observations of Psyche from the IUE showed a featureless UV spectrum from ∼220 to 320 nm, with some

possible narrow dips between 275 and 315 nm (Butterworth & Meadows 1985). The improved spectral resolution, high S/N of our HST observations, and the extension to ∼170 nm enable us to better characterize potential spectral features, as discussed below.

In Figure 6, we compare the HST data (binned to 1 nm) with the IUE data (created by digitizing Figure 5 from Butterworth & Meadows 1985), normalized at 255 nm, and find similar spectral slopes. The narrow features near >275 nm noted by Butterworth & Meadows (1985) may be those that are also observed in the HST data that we attribute to solar features. Another potential explanation for the high signal observed at 280 and 285 nm, though less likely, would be emission lines from Mg II and Mg I (Pickering et al. 1998) at Psyche. However, this would require a significant amount of sputtering of magnesium as well as the presence of a magnetic field to maintain an active aurora.

The IUE data exhibit a peak near 235–240 nm. The HST data similarly show an increase in albedo for several data points when binned to 1 nm, but we interpret that possible peak to be the edge of the 250 nm absorption feature when binned to 3 nm resolution, as shown in Figure 5.

4.4. FUV Upturn

At the FUV wavelengths, the spectra of the two hemispheres of Psyche reverse from a red (positive) slope to a blue (negative) slope. Due to the uncertainties in the data at wavelengths <180 nm, we cannot determine much about the FUV upturn, other than that the upturn begins near 200 nm during Visit 2 and closer to 180 nm for Visit 1 (Figure 3). This difference may be related to composition or processing of the surface, as discussed below.

UV spectral imaging is a demonstrated way to characterize space weathering of the Moon (Lucke et al. 1974) and asteroids (Hendrix & Vilas 2006; Vilas & Hendrix 2015). Spectral bluing in the UV has been attributed to space weathering of surfaces that cause changes to the properties of the surface material (Wagner et al. 1987). At wavelengths <180 nm, the observed albedo is due to surface scattering rather than volume scattering, and so the reflectance is related directly to the index of refraction, which increases with decreasing wavelengths for many materials (Henry et al. 1976; Hendrix & Vilas 2006). As a result, spectral inversions, where features that are relatively darker in the visible become UV-bright, have been noted on the Moon (Lucke et al. 1974; Seifert et al. 2014), Europa, (Roth et al. 2014; Becker et al. 2018), and Ganymede (Alday et al. 2017).

A similar FUV upturn was detected in UV data of the asteroid (1) Ceres (Hendrix et al. 2016), though the expected composition for the two asteroids are very different. Figure 7 shows the Ceres data normalized to Psyche's albedo. The NUV spectral slope of Psyche is redder than that of Ceres, and the 200 nm FUV upturn feature appears to be much broader or more gradual for Ceres. The Ceres data set included FUV observations from STIS (115–173 nm), enabling the characterization of the entire feature as an FUV "bump" that the authors attribute to highly processed (graphitized) carbons. Without the FUV data for Psyche and considering the level of noise <170 nm, it is difficult to assess whether the FUV upturn becomes a bump or if the spectrum continues to blue shortward of 170 nm.
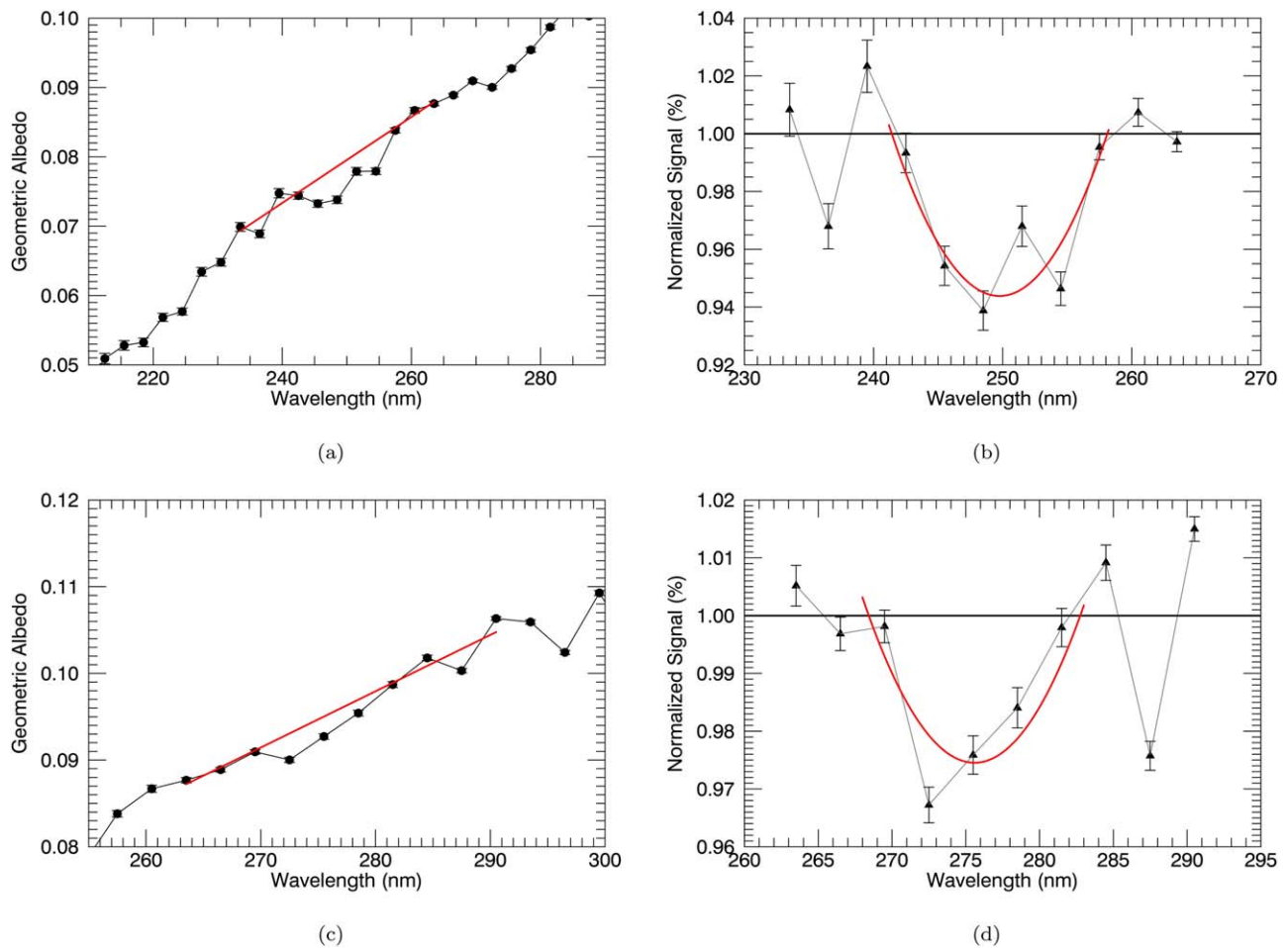
Figure 5. We remove the spectral continuum individually for each feature by fitting a line to the spectral region on either side of the feature ((a) and (c)). Then we fit a parabola to indicate the band center and depth for each feature ((b) and (d)); however, the 275 nm feature is more check mark-shaped than it is bowl-shaped.
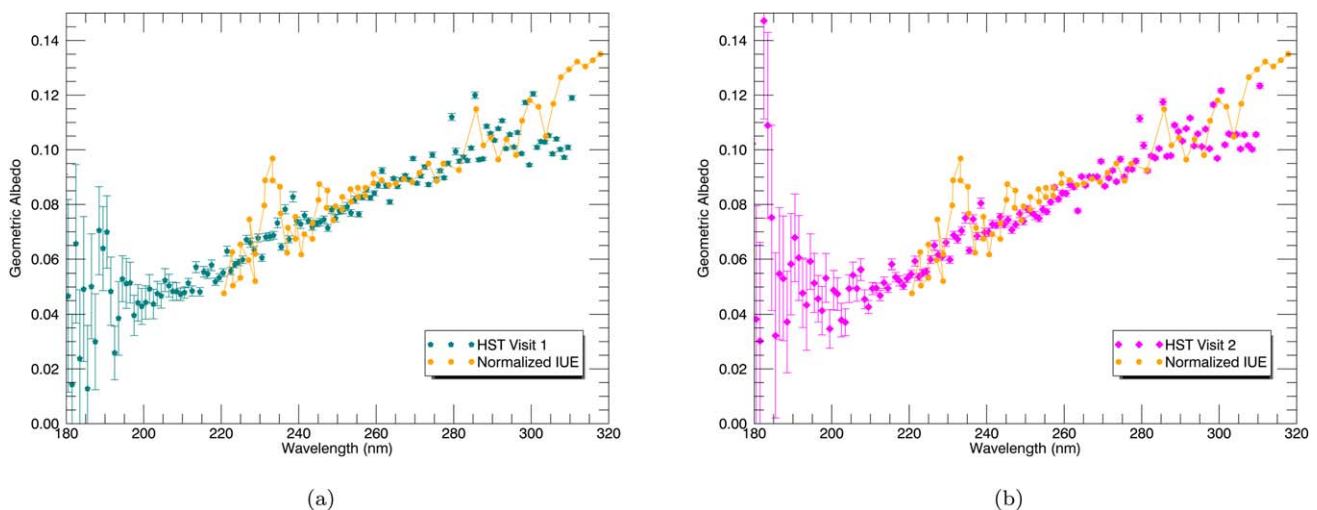

Figure 6. Comparison of the Psyche spectrum observed by the IUE as reported by Butterworth & Meadows (1985) normalized to the HST spectrum at 255 nm to compare with HST Visit 1 (left) and Visit 2 (right) binned to 1 nm.

5. Laboratory Data Comparisons

5.1. Meteorite and Analog Material Laboratory Spectra

We compare the observed spectrum of Psyche with laboratory measurements of various materials and meteorites that serve as potential analogs for the asteroid's composition.

We note, however, that the very sparse catalog of planetary body analogs measured at UV wavelengths limits the ability to definitively match any material or mixes of materials to the spectrum of Psyche.

Here we also include the visible spectrum of Psyche, using the data that were acquired from the Telescopio Nazionale
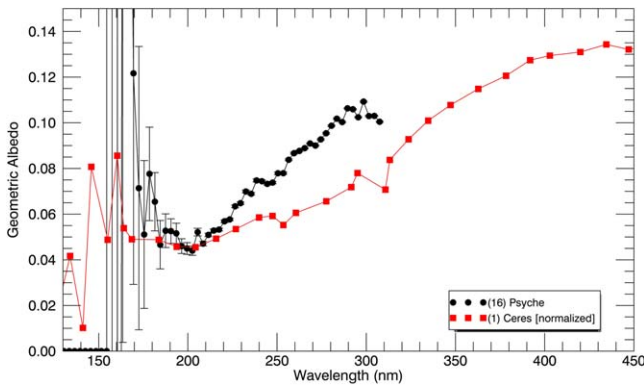
Figure 7. Asteroids (1) Ceres and Psyche both display an FUV upturn near 200 nm. Shortward of this feature, the spectral slope is blue rather than red. The width of the upturn for Ceres appears broader, and the overall slope of Ceres is less red. The Ceres data is from Hendrix et al. (2016) and was normalized to Psyche's albedo near 200 nm.

Galileo, the European Southern Observatory New Technology Telescope, and IRTF as reported by Fornasier et al. (2010) and from the Michigan–Dartmouth–MIT Observatory, reported by Binzel et al. (1995). We normalize the reported visible reflectances at 550 nm to the optical albedo of 0.15 determined by Shepard et al. (2017).

We compare the UV–visible (UV–Vis) spectrum of Psyche with the visible reflectance measurements of various materials obtained at the Reflectance Experiment Laboratory (RELAB) facility (RELAB 2006) at 30° phase, and the UV–Vis reflectance measurements from the Planetary Spectrophotometer Facility/HOSERLab described by Cloutis et al. (2008) and the atlas produced by Wagner et al. (1987), both using measurements near 0° phase. We also use optical constants with assumptions on particle sizes to derive reflectance spectra for some materials, as described in more detail in Section 5.2.

5.1.1. Iron

In Figure 8 we directly compare the UV–Vis reflectance of Psyche with the iron reflectance spectrum from Wagner et al. (1987), the ground metallic meteorite MET100 from the RELAB database (visible data) and the HOSERLab (UV–Vis data), and a reflectance spectrum of iron modeled using optical constants provided by Cahill et al. (2019) that is normalized at 220 nm and assuming the iron particles are 1 μm in size (see Section 5.2.2). The UV–Vis spectrum of Psyche is red, with a significantly steeper slope from 300 to 200 nm than at longer wavelengths (Figure 8). The downturn into the lower-albedo UV appears to begin around 400 nm. Additional reddening of Psyche's spectrum could be due to processes such as space weathering, which has been shown to alter surface spectra on some asteroid spectral types, especially at UV wavelengths.

We note the fairly good spectral fit across the UV and into the visible wavelengths for the iron spectrum derived from optical constants. We suggest the differences between this spectrum and the iron spectrum measured by Wagner et al. (1987) can be attributed to the laboratory technique used by Cahill et al. (2019) to prevent oxidation of the iron during the measurements. The overall shape of Psyche's spectrum is redder than the iron slab measured by Wagner et al. (1987). Similarly, the spectral slope of the crushed metallic meteorite is shallower than that of Psyche. However, the reflectance of the
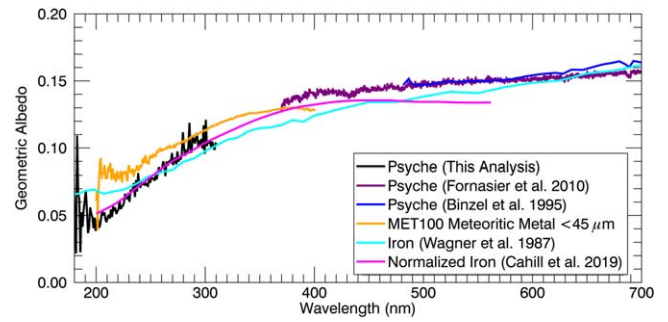

Figure 8. The geometric albedo of Psyche at UV and visible wavelengths. The spectra from Binzel et al. (1995) and Fornasier et al. (2010) are normalized to 0.15 at 550 nm. We compare Psyche's UV–Vis spectrum with that of iron from Wagner et al. (1987), the metallic meteorite from the HOSERLab database, and the iron model derived from the optical constants given by Cahill et al. (2019).

crushed meteorite and the iron slab are fairly close to the geometric albedo of Psyche.

5.1.2. Meteorites

We compare the spectrum of Psyche with all of the meteorite samples from the database described by Wagner et al. (1987) but do not find any strong matches. We note that there were no iron or stony iron meteorites in the catalog. In Figure 9, we show L, LL, H, and carbonaceous chondrites and find that the carbonaceous chondrites are significantly darker across the spectrum, with a much shallower slope in the UV than Psyche. This is not surprising, considering Psyche is not expected to be a carbonaceous asteroid. The L, LL, and H ordinary chondrites appear to be much more reflective in the visible than Psyche and display a very different spectral shape in the UV, with the exception of the H5 and H6 meteorites which match the overall shape of Psyche in the UV fairly well, but are again much brighter in the visible. Since the observed spectrum matches the highly metallic H chondrites better than the metal-poor L and LL chondrites, Psyche's composition may be consistent with mostly iron–nickel by mass.

Recent work (e.g., Landsman et al. 2017) found evidence that the uppermost regolith on Psyche is made of fine-grained silicates. This could suggest an enstatite chondrite analog for Psyche rather than an iron analog. In Figure 10 we compare Psyche with two enstatite chondrites and one aubrite (an E-type asteroid analog) but do not find that any of these highly reduced, iron-oxide-deficient meteorites represent good analogs for Psyche. However, we note that there are large differences between the spectra of these objects, and thus additional samples should be measured in the UV–Vis to determine if any enstatites or aubrites may serve as analogs to the UV spectrum of Psyche.

5.1.3. Planetary Surface Analogs

We look for signs of iron-oxide charge transfer bands and compare the spectra of Psyche with three possible surface materials from the HOSERLab database in Figure 11: olivine, orthopyroxene, and crushed meteoritic metal. Here we show the spectra for the smallest and largest particle sizes measured of olivine and orthopyroxene, specifically showing how the spectrum and absorption bands are affected by changes in the grain size.

The fine-grained olivine powder displays strong Fe^{2+}–O absorption features centered at 217 and 250 nm, which could correspond with the much weaker absorption features observed
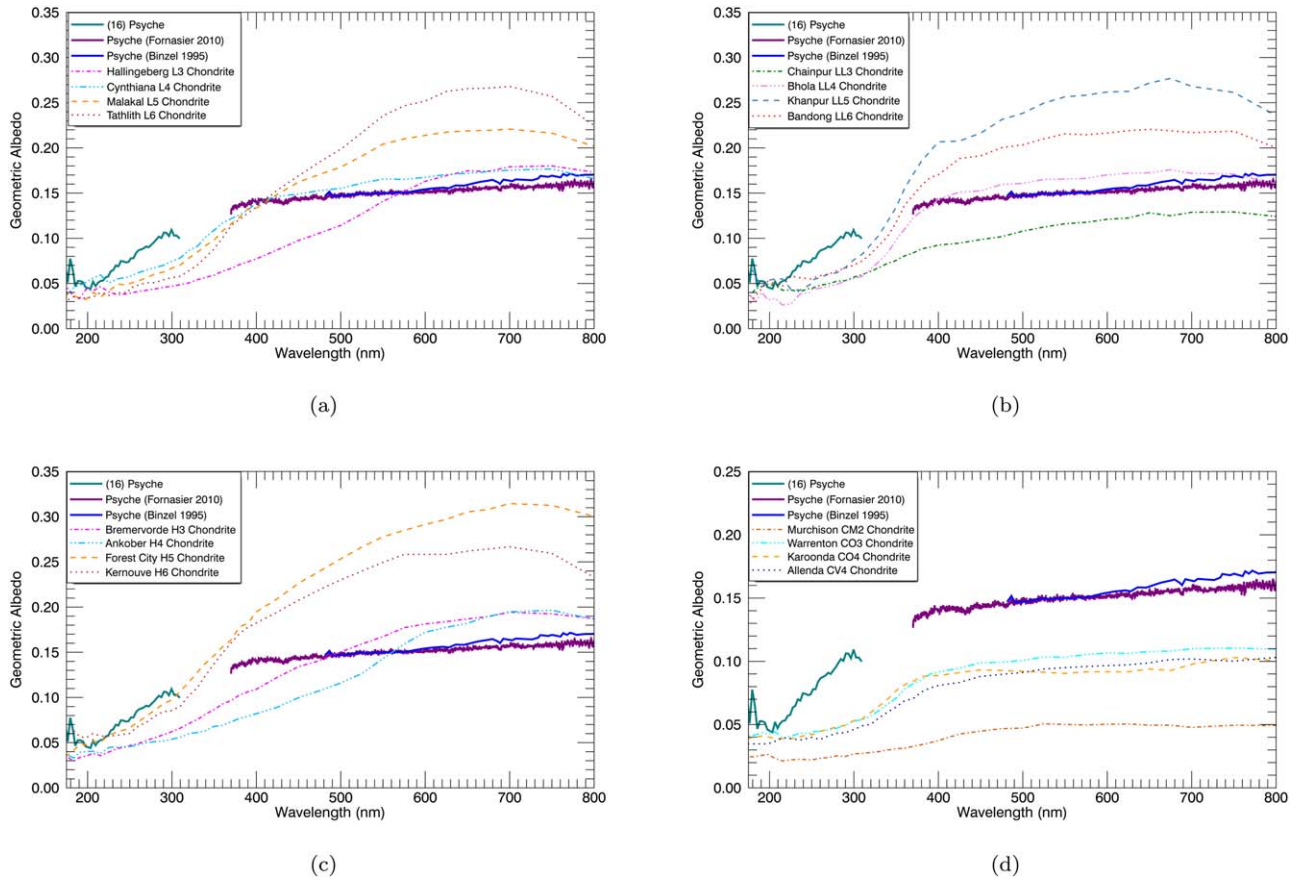
(a)

(b)

(c)

(d)

Figure 9. Comparison of the UV–Vis geometric albedo of Psyche with the lab-measured reflectances of L chondrites (top left), LL chondrites (top right), H chondrites (bottom left), and carbonaceous chondrites (bottom right).
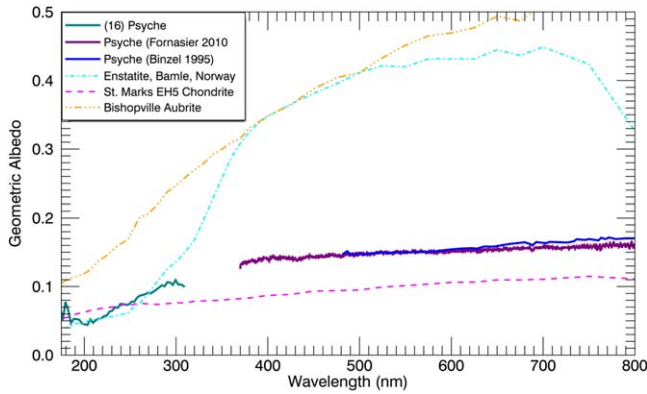

Figure 10. The albedo of Psyche compared with with the laboratory-measured reflectances of two enstatites and one aubrite, reported by Wagner et al. (1987).

in the Psyche spectrum. The meteoritic metal powder, which was observed in a way to minimize exposure to oxygen and therefore does not display metal-oxide absorption bands, is featureless and less red compared with the Psyche spectrum (as previously discussed). While the spectra of some of the high-calcium pyroxenes reported by Cloutis et al. (2008) also show absorption bands near 220 and 270 nm due to metal-oxide charge transfer absorptions, these features are much broader than features observed on Psyche. This does not rule out some orthopyroxene on the surface, as observed at longer wavelengths.

We note that Fornasier et al. (2010) also used the RELAB spectra and found the best-fit meteorite to be the iron meteorite
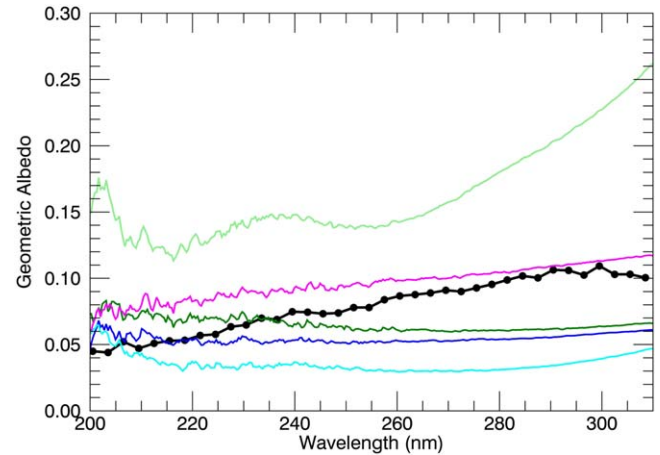
Figure 11. Comparison of Psyche albedo with HOSERLab spectra of crushed meteoritic metal, and the smallest and largest particle sizes measured for olivine and orthopyroxene (Cloutis et al. 2008).

MET101A, but this meteorite does not have UV lab observations available to compare with the new data presented in this paper.

5.2. Spectral Mixture Models

Like the albedo of Psyche, the spectrum of iron from the Wagner et al. (1987) database and the spectrum of iron derived from the optical constants given by Cahill et al. (2019) are fairly flat and featureless. The overall reflectance of the iron from
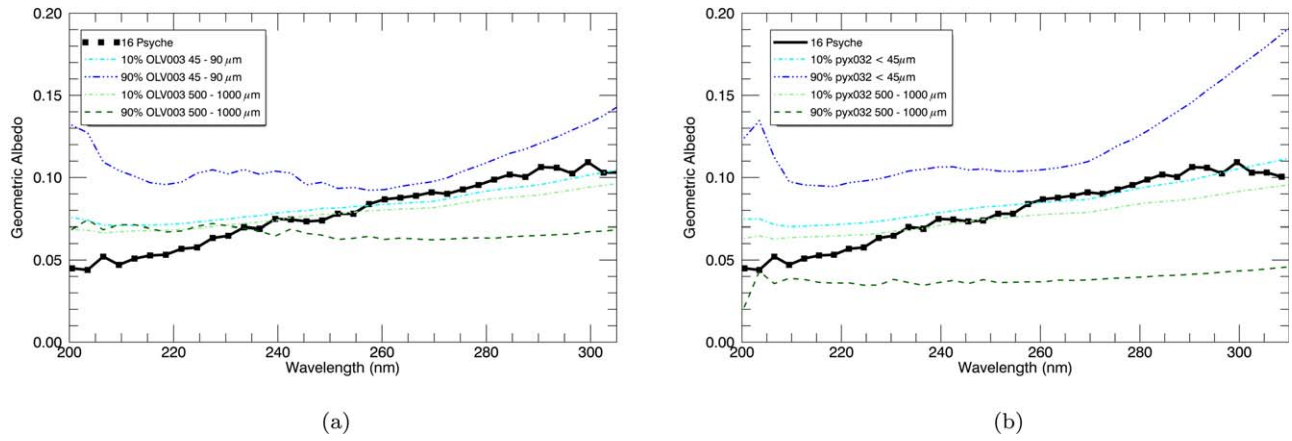
(a)

(b)

Figure 12. Linear mixture models of HOSERLab measurements of olivine powder mixed with iron. We show two particle size regimes (45–90 μm and 500–1000 μm) with an iron mixing ratio of 90:10 and 10:90.
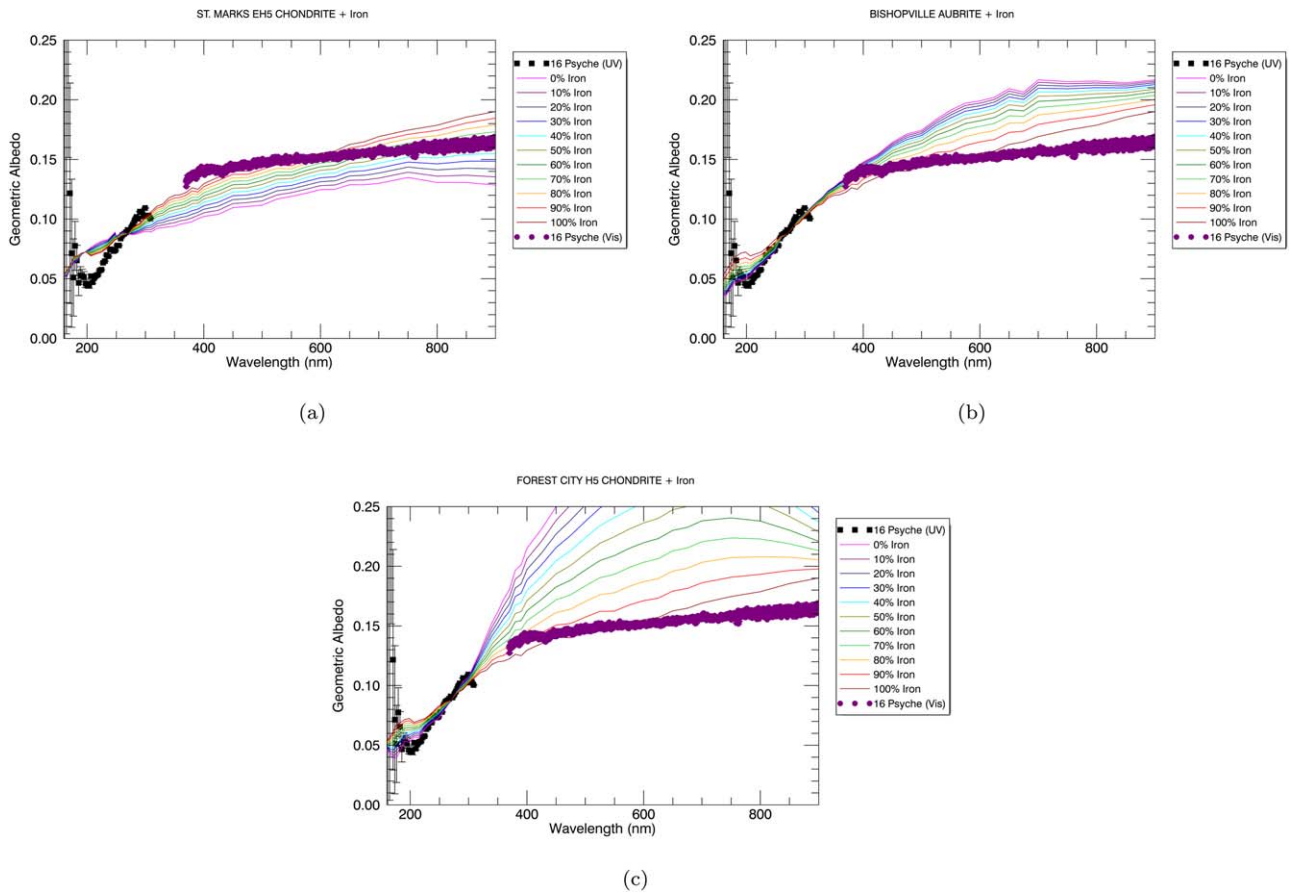

(a)

(b)

(c)

Figure 13. Linear mixture models of the EH5 enstatite (top left), an aubrite (top right), and the H5 ordinary chondrite (bottom) mixed with iron, normalized to the albedo of Psyche at 265 nm.

Wagner et al. (1987) is also similar to the asteroid's albedo. Since Psyche is expected to be primarily comprised of metals, it may be unsurprising that iron is a reasonable match. However, the spectra are not an exact match the the UV–Vis spectrum of Psyche and observations of the asteroid at longer wavelengths have shown that other materials such as orthopyroxenes are present as well.

5.2.1. Linear Mixture Reflectance Models

We attempt to match the spectrum of Psyche by creating linear mixture models of the materials discussed in Section 5.1 with the

iron spectrum from Wagner et al. (1987). These are simple models created by adding the two weighted spectra together.

In Figure 12, we show how a mixture of iron with two particle sizes regimes of olivine (left) and pyroxenes (right) compare with the UV spectrum of Psyche. The flat iron spectrum reduces any broad features observed in these materials and modifies the slope to be close to that of Psyche, though it is still not as steep.

In Figure 13 we show linear mixture models of iron mixed with the EH5 enstatite chondrite, the aubrite, and the H5 ordinary chondrite, normalized to the albedo of Psyche at 265 nm, which
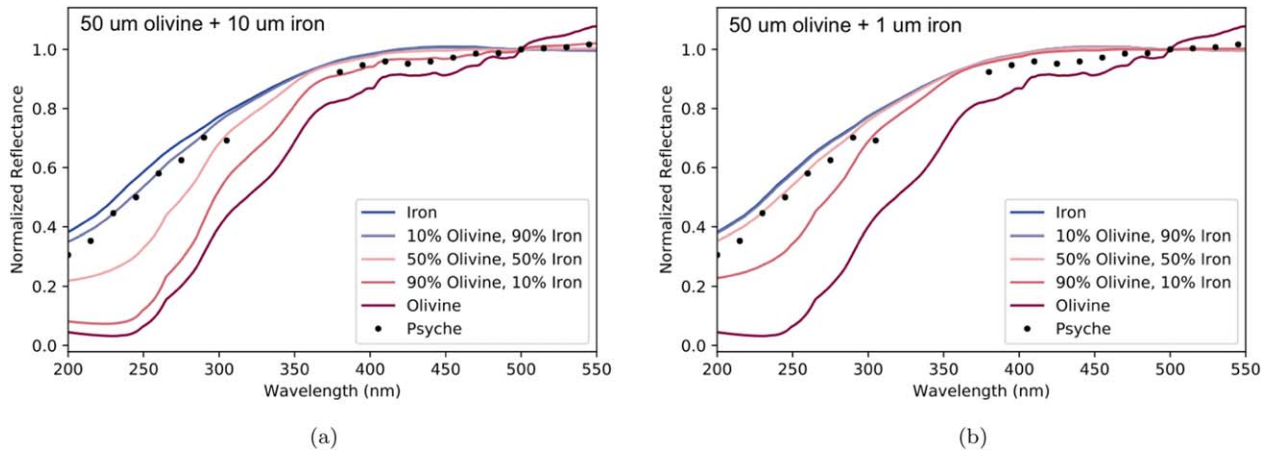
Figure 14. Intimate mixture reflectance model of iron and olivine, normalized to Psyche's spectrum at 500 nm. Decreasing the size of the iron grains increases its affect on the overall reflectance spectrum. Less iron overall is therefore needed to reproduce the shape of a reflectance spectrum similar to that of Psyche's. Note that in (b), the addition of 10% olivine is nearly indistinguishable from the pure iron.

was similar to the UV on its own in Figure 9. The modification of the spectra with the addition of iron often creates better, though still not good, matches to the spectrum of Psyche.

The mixture models show that the addition of iron to the meteorite spectra can improve how well they match the UV–Vis data of Psyche, though we do not find a satisfactory analog for the asteroid using any single material or mixture of materials. This is likely a result of several issues, including the extremely limited spectral database at UV wavelengths for the relevant materials and the sensitivity of the UV spectrum to the materials' grain sizes.

5.2.2. Intimate Mixture Reflectance Models

In the UV, the reflectance of materials is highly dependent on the particle grain sizes on the surface, in addition to how the materials are mixed. We assess the effect of grain sizes by comparing the reflectance spectra of intimate mixtures of iron and crystalline olivine. These intimate mixture models reflect localized mixing of the grains from the two different materials, rather than being spatially segregated, as is done for the linear mixture models. Work by Cloutis et al. (2015) show that the spectral characteristics of laboratory samples of olivine mixed with meteoritic metal are more strongly influenced by the metal if the materials are mixed intimately rather than linearly. We therefore expect these models to require less iron to approach Psyche's spectral shape than the linear mixtures shown above. The models described here use iron optical constants from Cahill et al. (2019) and optical constants for Stubachtal olivine from the Jena Database of Optical Constants for Cosmic Dust (https://www.astro.uni-jena.de/Laboratory/OCDB/newsilicates.html).

We produce the intimate mixture models using the disk-averaged form of Hapke's bidirectional reflectance model (Hapke 1981, 1984, 1986):

$$\left(\frac{I}{F}\right) = \left[\frac{\omega}{8}\{[1 + B(\alpha)]P(\alpha, g) - 1\} + \frac{r_0}{2}(1 - r_0)\right]$$
$$\times \left(1 - \sin\left(\frac{\alpha}{2}\right)\tan\left(\frac{\alpha}{2}\right)\ln\left[\cot\left(\frac{\alpha}{4}\right)\right]\right)$$
$$+ \left(\frac{2}{3}\right)r_0^2\left(\frac{\sin(\alpha) + (\pi - \alpha)\cos(\alpha)}{\pi}\right)K(\alpha, \bar{\theta}). \quad (2)$$

Here, α is the phase angle, ω is the single scattering albedo, and $r_0 = \frac{(1 - 1\sqrt{1 - \omega})}{(1 + \sqrt{1 - \omega})}$. For an intimate mixture, the single scattering albedo is a weighted average of the individual single scattering albedos of the constituent materials. The individual single scattering albedos are calculated from the optical constants of the materials, as described in detail by previous authors (e.g., Hendrix & Hansen 2008; Hapke 2012). We use a single-lobed Henyey–Greenstein phase function for $P(\alpha, g)$. Additional terms included in Equation (2) are: $B(\alpha)$, a correction for the shadow hiding opposition effect, and $K(\alpha, \bar{\theta})$, which corrects for large-scale surface roughness. The terms $P(\alpha, g)$, $B(\alpha)$, and $K(\alpha, \bar{\theta})$ require the additional Hapke parameters, g, B0, h, and $\bar{\theta}$. These would ideally be determined by a best fit to Psyche's full phase curve, but for these initial models we use values determined for asteroid (21) Lutetia (Masoumzadeh et al. 2015). Since we show only normalized reflectance spectra here we do not expect the use of the Lutetia Hapke constants to influence our interpretation of the models.

Figure 14 shows that as the grain size of iron decreases, the more dominant it becomes in the reflectance spectrum. At the 1 μm grain size, only ∼10% of the surface would need to be comprised of iron to still replicate the overall spectral shape of Psyche. If the grains are 10 μm in size, then a mixture closer to 50% iron and 50% olivine would be needed to still maintain the spectral shape.

This is especially true if the olivine grains are large. Figure 15 shows how changing the grain size of olivine effects the overall spectrum. If the olivine grains are large (>100 μm), the effect of the olivine on the overall reflectance spectrum is small. This means that olivine could make up anywhere between 10% and 90% of the mixture, but the spectrum would still be dominated by the small iron grains.

We use olivine rather than pyroxene in these models primarily because olivine optical constants in the UV–Vis spectral region are available in the Jena database of optical constants. We expect that the reflectance of an intimate mixture of pyroxene and iron would similarly be dominated by the iron spectrum. The strong influence of small iron grains, and the limited number of available optical constants for representative silicates, makes it difficult to quantify how much iron may be on the surface of Psyche if the regolith is intimately mixed.
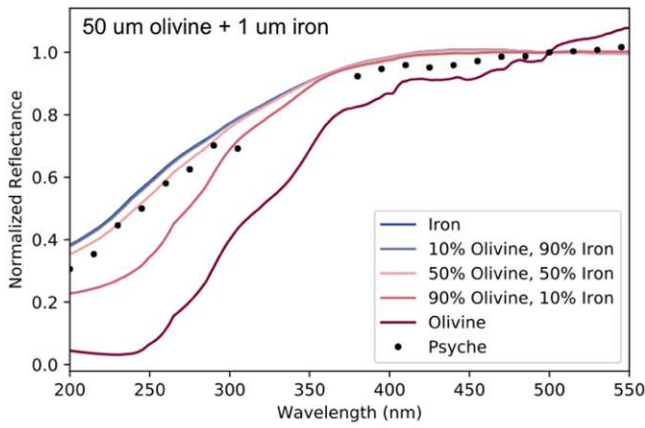
(a)
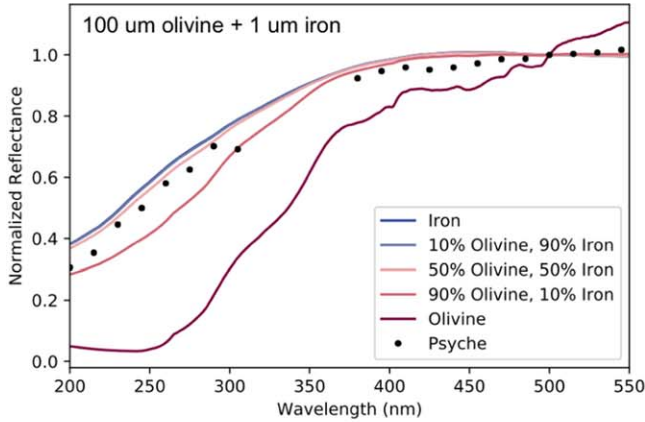
(b)
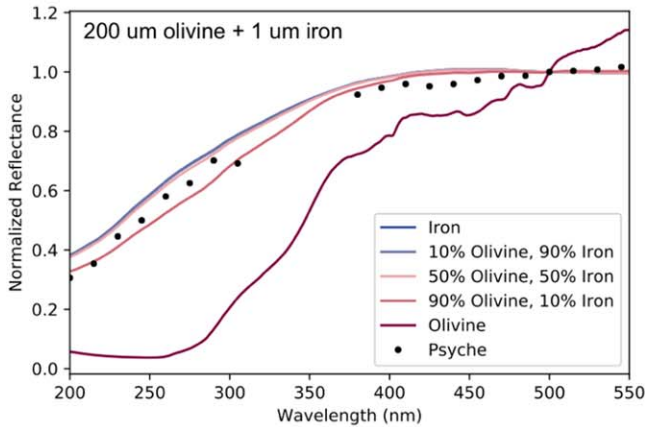
(c)

Figure 15. Intimate mixture reflectance models of iron and olivine, normalized to Psyche's spectrum at 500 nm. As the olivine grains are increased in size, their effect on the overall spectrum is weakened. Therefore, if the olivine grains are large, the material could dominate the mixture but the shape of the reflectance spectrum would still look similar to that of iron.

5.2.3. Intraparticle Mixture Reflectance Models

We also consider the case of intraparticle mixtures on the surface of Psyche. In this case, a small amount of one material is embedded in a matrix of the other material, resulting in spectral reflectance properties that differ from the intimate
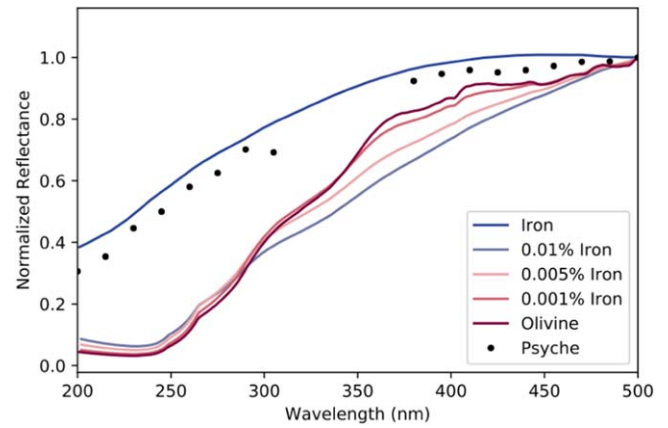
Figure 16. Intraparticle mixture reflectance models of olivine with varying amounts of contaminant iron, normalized to Psyche's spectrum at 500 nm. These models do not reproduce the overall shape of Psyche's spectrum.

mixture models. Here we assume the surface is primarily composed of 50 μm grains of olivine, with a percentage of iron contaminant trapped within those grains. This type of mixture has been previously used to model the effects of space weathering (e.g., Hapke 2001; Molyneux et al. 2020), which may lead to small inclusions of iron trapped within host regolith grains.

To produce these intraparticle mixture reflectance models, we use the Maxwell Garnett effective medium theory (Garnett 1904) to estimate combined optical constants for a small fraction of iron in an olivine matrix. We then use the combined optical constants to calculate the single scattering albedo, which is used with Equation (2) to produce a reflectance spectrum. The Maxwell Garnett theory is an approximation, and more exact models of space weathering effects based on the Mie theory have been developed (Lucey & Riner 2011; Penttilä et al. 2020). However, Penttilä et al. (2020) find that Maxwell Garnett models produce almost identical results to the more exact Mie simulations for small fractions of iron (0.01% or less) in olivine. We expect the models shown in Figure 16 to be valid approximations since they include only very small fractions of iron.

Figure 16 shows how the inclusion of different amounts of iron within the olivine matrix affects the reflectance spectrum. These mixtures do not reproduce the overall shape of Psyche's reflectance spectrum. This suggests that the iron that influences Psyche's UV reflectance is present as separate grains intimately or linearly mixed with silicates, rather than as inclusions in space-weathered grains. Adding more iron to the intraparticle models darkens the spectrum at $\lambda > 300$ nm and does not improve the fit to Psyche, although as noted above, these models are expected to be most accurate for the smallest fractions of iron.

6. Discussion

6.1. Implications from Spectral Analysis

Our spectral analysis shows that the northern hemisphere of Psyche may have a slightly lower albedo than the more equatorial region Figure 4. If this difference is real (i.e., not related to the geometry of the observation or topography of the asteroid), then this could have implications for additional variability on the surface of Psyche. As discussed above, the

grain sizes and/or small changes in the percentage of iron could impact the overall spectral shape and apparent brightness of the asteroid. The mid-UV is also sensitive to space weathering, which has been shown to become bluer with the asteroid's exposure time, depending on its spectral class, and therefore composition (Hendrix & Vilas 2006, 2019). A large spectroscopic survey of M-type asteroids that extends into the FUV would provide a more robust understanding of what happens to their surfaces in response to space weathering. If the differences on Psyche result from space weathering, then this may suggest a collisional history uncovering old or adding new material onto the asteroid's surface. Data collected by the Psyche mission may be able to distinguish whether these differences are caused by space weathering or are due to variations in the composition or grain size when it arrives at the asteroid in 2026.

In addition to the 0.9 μm feature attributed to pyroxene by Ockert-Bell et al. (2010), Fornasier et al. (2010) noted a weak absorption feature at 0.43 μm on Psyche (Figure 8) as well as five other M-types in their survey: (22) Kalliope, (69) Hesperia, (216) Kleopatra, (338) Budrosa, and (498) Tokio. They acknowledge the difficulty in attributing this feature and suggest it could be associated with chlorites and Mg-rich serpentines as suggested for enstatite chondrites (King & Clark 1989), pyroxene minerals such as pigeonite or augite (Busarev 1998), or an Fe^{3+} spin-forbidden transition in the iron sulfate jarosite suggested for low-albedo asteroids (Vilas et al. 1993). We note that jarosite (as well as other sulfates such as gypsum and hexahydrite) were explicitly measured in the UV by Cloutis et al. (2008). The jarosite spectrum was noted to be unlike other minerals in the study, with minima near 225, 262, and 240 nm, which are attributable to Fe^{3+}–O charge transfers. The jarosite also produces a very dark spectrum (<5% reflectance) out to 400 nm, which is inconsistent with the observed spectrum of Psyche.

Cloutis et al. (2008) notes that the strongest Fe^{3+}–O and Fe^{2+}–O charge transfer bands occur near 217 and 250 nm, respectively, with Fe^{3+}–O absorption roughly two orders of magnitude more intense than the other. However, we detect only a weak absorption feature at 250 nm. If the 217 nm feature is present, it is obscured by the spectral slope and the FUV upturn at slightly shorter wavelengths. This may suggest that only Fe^{2+} is present, that the FUV upturn is in fact a deep Fe^{3+} absorption feature, or that there are no charge transfer bands present and that the observed features may be caused by other mineral properties.

When comparing the slopes of some materials, Cloutis et al. (2008) found that for low-iron olivine, the ratio of 400 nm:250 nm is 4.57 versus 1.47 for meteoritic metal for grain sizes <45 microns. The 400 nm : 250 nm ratio for Psyche, including data from Fornasier et al. (2010), is close to 2.0, making it significantly less red-sloped than the low-iron olivine, potentially ruling out significant amounts of low-iron olivine on the surface of Psyche.

In this work we show that the reflectance of the pure laboratory-measured irons (Wagner et al. 1987; RELAB 2006; Cloutis et al. 2008) are consistent with the albedo of Psyche, and although the linear and intimate mixture models can closely replicate the shape of the spectrum, some normalization is needed to match the albedo. This is in part due to the spectrum's dependence on grain sizes. For example, if the iron grains are small, they may dominate the spectral signal for a variety of mixes of surface materials even if the iron is present
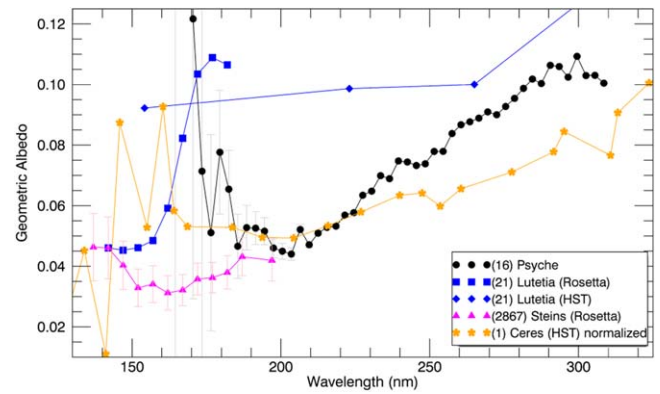

Figure 17. Comparison of the geometric albedos for Psyche with Rosetta Alice observations of (2867) Šteins (purple triangles) and (21) Lutetia (blue squares), HST observations of (21) Lutetia (blue diamonds), and HST STIS observations of (1) Ceres (orange stars). These are the only four asteroids studied at wavelengths <220 nm, and their spectra appear very different from one another at these wavelengths.

in small amounts. Matching the absolute albedo rather than the spectral shape would further constrain the composition but it requires additional knowledge about the Hapke parameters, but to refine those, we need more UV observations at a range of phase angles.

6.2. Asteroids in the UV

Only four asteroids have been studied at wavelengths <220 nm. In Figure 17, we compare the geometric albedo of the asteroids Psyche (this study), the M-type asteroid (21) Lutetia observed by the Alice instrument on the Rosetta spacecraft (A'Hearn et al. 2010) and photometrically by HST (Weaver et al. 2010), the E-type asteroid (2867) Šteins observed by Rosetta Alice (Stern et al. 2011), and the C-type asteroid (1) Ceres from HST STIS observations (Hendrix et al. 2016). None of their spectra at these wavelengths appear to be similar; it is possible that observations at these wavelengths could be highly diagnostic of either surface compositions or differences in the space weather processing of minor planets.

Unlike Psyche, (21) Lutetia has a relatively high albedo between 200 and 260 nm, with a strong absorption feature shortward of 180 nm. This feature is consistent with laboratory data and computer models of water ice (Hendrix & Hansen 2008), which may support the classification by Rivkin et al. (2000) of (21) Lutetia as a W-class asteroid, a subset of M-types that exhibit a strong 3 μm absorption feature attributed to hydration. However, H_2O absorption features at IR wavelengths were not detected by Rosetta Visible and Infrared Thermal Imaging Spectrometer (VIRTIS; Coradini et al. 2011) during its flyby of the asteroid. Stern et al. (2011) attribute the strong spectral feature to SO_2, though they note it is unlikely for it to exist on the asteroid. Again, expanding the laboratory database in the UV may reveal other materials with this distinctive reflectance property that could be used to constrain the composition of planetary bodies.

The UV spectra of Psyche (though noisy shortward of 180 nm) do not appear to exhibit the sharp edge near 165 nm that would be attributed to water ice. This may support the interpretation by Takir et al. (2017) that the 3 μm feature on Psyche could suggest the presence of hydroxyl rather than water near the surface. Instead, the spectra of Psyche become blue at wavelengths <200 nm, similar to the spectra of (1)

Ceres (Hendrix et al. 2016), though the NUV spectra of Psyche are redder than those of (1) Ceres. Observations at FUV wavelengths would show whether Psyche's spectrum displays a similar FUV "bump" as well and would have significant implications for the composition of the asteroid since that feature was attributed to graphite for (1) Ceres.

Though it is difficult to directly compare Psyche with the E-type asteroid (2867) Šteins due to a lack of good overlapping spectral data, the geometric albedos of the two asteroids appear to be very similar near 200 nm. This may have interesting implications for the composition of Psyche, which has been compared to E-type asteroids as well. However, there appears to be a bluing of Psyche's spectrum below 200 nm that is not present on Šteins. More data of Psyche at shorter wavelengths would enable a direct comparison with the E-type asteroid and establish spectral similarities or differences not only between these specific asteroids but also the M and E classes of asteroids.

After multiple bandpass high-resolution spectral observations, the asteroids designated to the umbrella X-class by the Eight Color Asteroid Survey (Tholen 1984) were further classified into E-, P-, and M-types, which have also since been further split due to intrinsic differences in the spectra, suggesting distinct origins, compositions, or both. UV observations of these classes of asteroids offer new and critical insight into the composition of these objects that can reduce the degeneracy of spectra at longer wavelengths. This may be especially true for distinguishing the source of the 3 μm absorption feature between hydroxyl and water.

7. Summary

We report the UV observations of the asteroid Psyche from 170 to 310 nm. The UV spectrum is much redder than in the visible spectrum, consistent with previous IUE observations of the asteroid. We did not find significant spectral variations with rotation, though the equatorial region of the asteroid may have a higher overall reflectance than the northern hemisphere. We report weak absorption features near 250 and 270 nm, which may be attributed to iron-oxide charge transfer bands. The spectrum displays an FUV upturn at wavelengths <200 nm, which may have implications for space weathering.

Due in part to the very limited spectral reflectance database in the UV, we do not find any strong analogs to Psyche in the UV. The enstatite chondrites for which UV observations exist do not serve as good UV–Vis analogs for Psyche. Pure iron or linear mixture models with materials mixed with significant amounts of iron reproduce the overall shape of Psyche in the UV and visible wavelengths better than any tested material alone. Intimate mixture reflectance models assuming 1 μm iron grains mixed with olivine show that even small amounts of iron (~10%) can reproduce the overall shape of Psyche's spectrum, making it difficult to quantify the amount of iron that may be present on the surface of Psyche.

More UV laboratory work is needed to produce a robust library from which the composition of, and space weathering effects on, planetary bodies can be better constrained. Bidirectional reflectance distribution function UV lab measurements will be especially useful for future modeling of the spatial variations along the slit for the different hemispheres viewed by HST here and in future observations. The diversity of spectral features and slopes observed in the four asteroids studied at FUV and mid-UV wavelengths implies that there is still much that can be learned about asteroid surfaces through their examination in the UV spectrum.

ORCID iDs

Tracy M. Becker https://orcid.org/0000-0002-1559-5954
Nathaniel Cunningham https://orcid.org/0000-0002-8957-7310
Philippa Molyneux https://orcid.org/0000-0002-4725-4775
Lorenz Roth https://orcid.org/0000-0003-0554-4691
Lori M. Feaga https://orcid.org/0000-0002-4230-6759
Kurt D. Retherford https://orcid.org/0000-0001-9470-150X
Zoe A. Landsman https://orcid.org/0000-0003-4980-1135
Linda T. Elkins-Tanton https://orcid.org/0000-0003-4008-1098

References

A'Hearn, M. F., Feaga, L. M., Bertaux, J.-L., et al. 2010, P&SS, 58, 1088
Alday, J., Roth, L., Ivchenko, N., et al. 2017, P&SS, 148, 35
Asphaug, E. 2010, ChEG, 70, 199
Asphaug, E., Agnonr, C. B., & Quentin, W. 2006, Natur, 439, 155
Becker, T. M., Retherford, K. D., Roth, L., et al. 2018, JGRE, 123, 1327
Bell, J. F., Davis, D. R., Hartmann, W. K., & Gaffey, M. J. 1989, in Asteroids II, ed. R. P. Binzel, T. Gehrels, & M. S. Matthews (Tucson, AZ: Univ. Arizona Press), 921
Binzel, R. P., Bus, S. J., Xu, S., et al. 1995, Icar, 117, 443
Britt, D. T., & Consolmagno, G. J. 2003, M&PS, 28, 1161
Busarev, V. V. 1998, Icar, 131, 32
Butterworth, P. S., & Meadows, A. J. 1985, Icar, 62, 305
Cahill, J. T. S., Blewett, D. T., Nguyen, N. V., et al. 2019, Icar, 317, 229
Carry, B. 2012, P&SS, 73, 98
Chapman, C. R., & Salisbury, J. W. 1973, Icar, 19, 507
Cloutis, E. A., McCormack, K. A., Bell, J. F., et al. 2008, Icar, 197, 321
Cloutis, E. A., Sanchez, J. A., Reddy, V., et al. 2015, Icar, 252, 39
Coradini, A., Capaccioni, F., Erard, S., et al. 2011, Sci, 334, 492
DeMeo, F. E., Binzel, R. P., Slivan, S. M., & Bus, S. J. 2009, Icar, 202, 160
Elkins-Tanton, L. T., Bell, J. F., III, Asphaug, E., et al. 2017, in European Planetary Science Congress, ESPC2017-384 11 (Riga, Latvia)
Fornasier, S., Clark, B. E., Dotto, E., et al. 2010, Icar, 210, 655
Garnett, J. C. M. 1904, RSPTA, 203, 385
Hanuš, J., Viikinoski, M., Marchis, F., et al. 2017, A&A, 601, A114
Hapke, B. 1981, JGR, 86, 3039
Hapke, B. 1984, Icar, 59, 41
Hapke, B. 1986, Icar, 67, 264
Hapke, B. 2001, JGR, 106, 10039
Hapke, B. 2012, Theory of Reflectance and Emittance Spectroscopy (2nd ed.; Cambridge: Cambridge Univ. Press)
Hardersen, P. S., Gaffey, M. J., & Abell, P. A. 2005, Icar, 175, 141
Hendrix, A. R., & Hansen, C. J. 2008, Icar, 193, 323
Hendrix, A. R., & Vilas, F. 2006, AJ, 132, 1396
Hendrix, A. R., & Vilas, F. 2019, GeoRL, 46, 14307
Hendrix, A. R., Vilas, F., & Li, J.-Y. 2016, GeoRL, 43, 8920
Henry, R. C., Fasti, W. M. G., Lucke, R. L., & Hapke, B. W. 1976, Moon, 15, 51
Kaasalainen, M., Torppa, A., & Piieronen, J. 2002, Icar, 159, 369
King, T. V. V, & Clark, R. N. 1989, JGR, 94, 13997
Kuzmanoski, M., & Kovačević, A. 2002, A&A, 395, L17
Landsman, Z. A., Campins, H., Pinilla-Alonso, N., Hanuš, J., & Lorenzi, V. 2015, Icar, 252, 186
Landsman, Z. A., Emery, J. P., Campins, H., et al. 2017, Icar, 304, 58

Lucey, P. G., & Riner, M. A. 2011, Icar, 212, 451
Lucke, R. L., Henry, R. C., & Fastie, W. G. 1974, LPSC, 5, 469
Lupishko, D. F., Kiselev, N. N., CHernova, G. P., & Bel'skaya, I. N. 1980, AIP
    Sov. Astron. Let, 6, 102
Marciniak, A., Bartczak, P., Santana-Ros, T., et al. 2012, A&A, 545, A131
Masoumzadeh, N., Boehnhardt, H., Li, J.-Y., & Vincent, J.-B. 2015, Icar,
    257, 239
Matter, A., Delbo, M., Benoit, C., & Ligori, S. 2013, Icar, 226, 419
McClintock, W. E., Rottman, G. J., & Woods, T. N. 2005, SoPh, 230, 225
Molyneux, P., Nichols, J., Becker, T. M., Raut, U., & Retherford, K. D. 2020,
    JGRE, 125, e06476
Ockert-Bell, M. E., Clark, B. E., Shepard, M. K., et al. 2010, Icar, 210, 647
Ostro, S. J., Campbell, D. B., & Shapiro, I. I. 1985, Sci, 229, 442
Penttilä, A., Väisänen, T., Markkanen, J., et al. 2020, Icar, 345, 113727
Pickering, J. C., Thorne, A. P., & Webb, J. K. 1998, MNRAS, 300, 131
RELAB 2006, Reflectance Experiment Laboratory User's Manual (Providence,
    RI: Dept. of Geological Sci, Brown Univ.)
Rivkin, A. S., Howell, E. S., Lebofsky, L. A., Clark, B. E., & Britt, D. T. 2000,
    Icar, 145, 351
Roettger, E. E., & Buratti, B. J. 1994, Icar, 112, 496
Roth, L., Saur, J., Retherford, K. D., et al. 2014, Sci, 242, 171

Sanchez, J. A., Reddy, V., Shepard, M. K., et al. 2017, AJ, 153, 29
Sarid, G., Stewart, S. T., & Leinhardt, Z. M. 2015, in IAU General Assembly
    Meeting 29, 2256152
Seifert, C. M., Mandt, K. E., Retherford, K. D., et al. 2014, in 45th Lunar and
    Planetary Science Conf. Abstract (Woodlands, TX), 1191
Shepard, M. K., Clark, B. E., Ockert-Bell, M., et al. 2008, Icar, 195, 184
Shepard, M. K., Clark, B. E., Ockert-Bell, M., et al. 2010, Icar, 208, 221
Shepard, M. K., Richardson, J., Taylor, P. A., et al. 2017, Icar, 218, 388
Sparn, T. P., Rottman, G., Woods, T. N., et al. 2005, Sol. Phys., 230, 71
Stern, S. A., Parker, J. Wm., Feldman, P. D., et al. 2011, AJ, 141, 199
Takir, D., Reddy, V., Sanchez, J. A., Shepard, M. K., & Emery, J. P. 2017, AJ,
    153, 31
Tholen, D. J. 1984, PhD thesis, Univ. Arizona, Tucson
Usui, F., Hasegawa, S., Ootsubo, T., & Onaka, T. 2019, PASJ, 71, 1
Viateau, B. 2000, A&A, 354, 725
Viikinkoski, M., Vernazza, P., Hanuš, J., et al. 2018, A&A, 691, L3
Vilas, F., Hatch, E. C., Larson, S. M., Sawyer, S. R., & Gaffey, M. J. 1993,
    Icar, 102, 225
Vilas, F., & Hendrix, A. R. 2015, AJ, 150, 64
Wagner, J. K., Hapke, B. W., & Wells, E. N. 1987, Icar, 69, 14
Weaver, H. A., Feldman, P. D., Merline, W. J., et al. 2010, A&A, 518, A4